Memo version 1.0

BESIII Analysis Memo

DocDB-XXX

BAM-XXX

January 18, 2022

Study of $\chi_{cJ} \to p\bar{p}K^+K^-$

Lu liu[a], Shuangshi Fang[b], Chunxu Yu[a], and Aiqiang Guo[c]

[a]*Nankai University*
[b]*Institute of High Energy Physics, CAS*
[c]*Institute of Modern Physics, CAS*

Internal Referee Committee

Ref1 xx (Chair)[d], Ref2 xx[e], and Ref3 xx[f]

[d]*XXX*
[e]*XXX*
[f]*XXX*

DocDB : http://docbes3.ihep.ac.cn/cgi-bin/DocDB/ShowDocument?docid=XXX

Hypernews : http://hnbes3.ihep.ac.cn/HyperNews/get/paperXXX.html

Abstract

Based on 448.1×10^6 $\psi(2S)$ events collected from the BESIII detector, the decays $\chi_{cJ} \to p\bar{p}K^+K^-(J = 0, 1, 2)$ are studied and updated via the radiative transition $\psi(2S) \to \gamma\chi_{cJ}$. The decay branching factions of $\chi_{cJ} \to p\bar{p}K^+K^-$, $\chi_{cJ} \to p\bar{p}\phi$, $\chi_{cJ} \to pK^-\bar{\Lambda}(1520) + c.c.$ and $\chi_{cJ} \to \Lambda(1520)\bar{\Lambda}(1520)$ decay modes are improved, among them, the upper limit results of $\chi_{c1} \to p\bar{p}\phi$ and $\chi_{c1} \to \Lambda(1520)\bar{\Lambda}(1520)$ are set to be B $(\chi_{c1} \to p\bar{p}\phi)$<$1.44 \times 10^{-5}$ and B $(\chi_{c1} \to \Lambda(1520)\bar{\Lambda}(1520))$<$0.71 \times 10^{-4}$ at 90% confidence level, respectively. In addition, the evidence of the decay $\chi_{c1} \to p\bar{p}\phi$ is observed for the first time and the corresponding branching faction is measured to be $(1.11 \pm 0.30 \pm 0.27) \times 10^{-5}$. The uncertainties are statistical and systematic, respectively.

Contents

1 Introduction

As we all know, the heavy-quark mass provides a natural boundary between the perturbative and non-perturbative regimes. Quarkonium systems are deemed as a distinctive laboratory to study the interplay between perturbative and non-perturbative effects in quantum chromodynamics(QCD). Charmonium states are mesons formed by a bound state of a charm quark and a charm anti-quark. In 1974, the first excited state of charmonium J/ψ boson was discovered in experiments [1–3]. Thereafter, more and more charmonium states have been discovered, etc. $\psi(3686)$(the so-called $\psi(2S)$), $\psi(3770)$ and so on. In the quark model, the χ_{cJ} $(J = 0, 1, 2)$ mesons are the $3P_J$ charmonium states. Their decays are experimentally and theoretically not as well studied as the vector charmonium states J/ψ and $\psi(2S)$. Unlike the J/ψ and $\psi(2S)$, the P-wave charmonia states χ_{cJ} $(J = 0, 1, 2)$ are not directly produced in e^+e^- collisions, thus people don't have a deep understanding of this until today. Very clean environment for the study of χ_{cJ} $(J = 0, 1, 2)$ states is important for a better understanding of their nature and decay mechanisms, as well as for testing QCD-based calculations because it can be generated in radiative decays $\psi(2S) \to \gamma\chi_{cJ}$. Recent theory indicates that the color octet mechanism [4] could have large contributions to the decays of the P-wave charmonium states. However, these calculations, as well as experimental measurements still have large errors, for example, branching fraction of $\chi_{c1} \to p\bar{p}\phi$ and $\chi_{c1} \to \Lambda(1520)\bar{\Lambda}(1520)$ are the results of upper limit from particle data group (PDG) [5] till now. Therefore, more precise experimental data besides more theoretical efforts are crucial to deepen the dynamic mechanism of χ_{cJ} decay. Getting more experimental data seems particularly important.

In this paper, by using the world largest $\psi(2S)$ sample taken at the center-of-mass energy of $\sqrt{s}$ = 3.686 GeV with the Beijing Spectrometer III (BESIII) detector, we present the first measurement of the branching fraction of $\chi_{c1} \to p\bar{p}\phi$ and $\chi_{c1} \to \Lambda(1520)\bar{\Lambda}(1520)$. Besides, the branching fraction precision of other decay modes of χ_{cJ} are improved.

2 BESIII detector, data and Monte Carlo

2.1 BESIII detector

The BESIII detector [6] at the double-ring Beijing Electron-Positron Collider (BEPCII) is a major upgrade of the BESII experiment at the single-ring Beijing Electron-Positron Collider (BEPC) [7] for studying physics in the τ-charm energy region [8]. The designed peak luminosity of BEPCII is 1.0×10^{33} $\mathrm{cm}^{-2}\mathrm{s}^{-1}$ at a beam current of 0.93 A which is optimized at the energy of $\psi(3770)$ peak. The BESIII detector has a geometrical acceptance of 93% of 4π solid angle and consists of the following main components.

- A small-celled main drift chamber (MDC) with 43 layers providing an average single-hit resolution of 135 μm is used to track charged particles, and the momentum resolution of the charged particle in a 1.0 T magnetic field is 0.5% at 1 GeV/c.

- An electromagnetic calorimeter (EMC) made of 6240 CsI (Tl) crystals arranged in a cylindrical shape (barrel) plus two end caps is used to measure photon energy and position information. For 1.0 GeV photons, the energy resolution is 2.5% in the barrel and 5% in the end-caps, and the position resolution is 6 mm for the barrel and 9 mm for the end caps.

- A time-of-flight system (TOF) constructed of 5 cm thick plastic scintillators, with 176 detectors of 2.4 m length in two layers in the barrel and 96 fan-shaped detectors in the endcaps is used for particle identification (PID). The barrel (end-caps) time resolution of 80 (110) ps provided 2σ K/π separation for momenta up to $\sim$ 1.0 GeV/c.

- A muon chamber system for muon detection made of resistive plate chambers arranged in 9 layers in the barrel and 8 layers in the end-caps provides 2 cm position resolution.

2.2 Data sets

The result reported in this analysis is based on the data sample taken at the $\psi(2S)$ with the BESIII detector during 2009 and 2012. The total number of $\psi(2S)$ events is $(448.1 \pm 2.9) \times 10^6$, which have been determined with inclusive hadronic events as described in Ref. [9].

2.3 Monte Carlo Simulation

2.3.1 Simulation Tools and Simulation Environment

The optimization of event selection and estimation of physics backgrounds are performed through Monte Carlo (MC) simulations of background and signal. The GEANT4-based [10] simulation software BOOST [11]

includes the geometric and material description of the BESIII detectors, the detector response and digitization models, as well as the tracking of the detector running conditions and performance. The production of the $\psi(2S)$ resonance is simulated by the MC event generator KKMC [12], while the decays are generated by EVTGEN [13] for known decay modes with branching ratios being set to the PDG [5] world average values, and by LUNDCHARM [14] for the remaining unknown decays.

This analysis is performed on the framework of the BESIII Offline Software System (BOSS) [15] and the version is BOSS 6. 6. 4. p03.

2.3.2 Simulation for signal / data Events

Several exclusive MC samples are used to determined detection efficiencies or study main background sources. For each decay, 2.24×10^5 MC events are generated. The $\psi(2S) \to \gamma\chi_{cJ}(J = 0, 1, 2)$ decays are modeled with P2GCJ($J = 0, 1, 2$) models [16]. The decays $\chi_{cJ} \to p\bar{p}\phi$, $\chi_{cJ} \to p\bar{p}K^+K^-$, $\chi_{cJ} \to pK^-\bar{\Lambda}(1520)$, $\chi_{cJ} \to \Lambda(1520)\bar{p}K^+$, $\chi_{cJ} \to \Lambda(1520)\bar{\Lambda}(1520)$, $\Lambda(1520) \to pK^-$ and $\bar{\Lambda}(1520) \to \bar{p}K^+$ are generated using the phase space (PHSP) model. The decay $\phi \to K^+K^-$ is generated using the VSS model.

About 506 million inclusive MC sample is used to investigate possible backgrounds, of which the branching fractions of the known physics processes are set to world average values according to PDG [5].

3 Event selection

The criteria of event selection for good candidates are discussed in the following aspects.

- For charged tracks, there are several general criteria. Charged tracks detected in the MDC must satisfy |cos θ|< 0.93, where θ is the polar angle with respect to positron beam direction. $V_r < 1.0$ cm and $V_z < 10$ cm are performed, where V_r and V_z are the closest approach distance from the beam line to the reconstructed track in x-y and z direction, respectively. There should be two positive and two negative charged tracks which are selected for further selection. The total net charge is 0.

- A photon is marked as a photon candidate if it satisfies: $0 \leq T_{TDC} \leq 14$ (with a unit of 50ns), TDC is the time information of EMC; $E_\gamma \geq 25$ MeV for barrel EMC ($|cos\theta|< 0.80$), $E_\gamma \geq 50$ MeV for endcap EMC ($0.86 < |cos\theta|< 0.92$). The opening angel between a shower and the nearest charged track should be no less than 10, the isolation angle is calculated by the angle between the position of the center crystal of the shower and the extrapolated position on EMC of the charged track.

- Particle identification (PID) is used to identify the charged tracking and the selection criteria are $prob(p) > prob(K)$, $prob(p) > prob(\pi)$ for proton and $prob(K) > prob(p)$, $prob(K) > prob(\pi)$ for kaon. Totally, we identify a proton, an anti-proton, two kaons in one event, and keep the total charges are zero.

- A vertex fitting is performed on the four tracks to ensure that they originate from the interaction point.

- The four-constraint energy-momentum conservation kinematic fit (4C fit) is used to the final state $\gamma p\bar{p}K^+K^-$. All the tracks should be fulfill the 4C kinematic fit and the kinematic fit constrained by the initial $\psi(2S)$ four-momentum is performed under the final state hypothesis $\gamma K^+K^-p\bar{p}$. The χ^2_{4c} is required to be less than 200. If there're more than one good photon, the combination with least χ^2 is chosen.

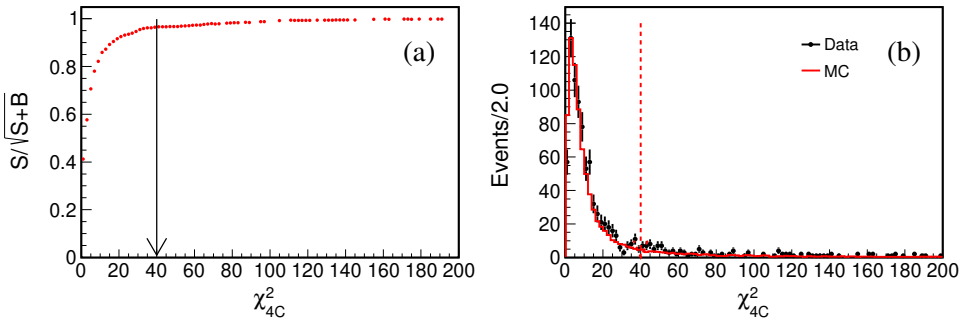

Figure 1: (a) The optimization of χ^2_{4c} for χ_{c0}. (b) The distribution of χ^2_{4c} , where dots with error bars are data and the red histograms represent the signal MC for χ_{c0}.

4 Analysis of χ_{cJ} decaying into $p\bar{p}K^+K^-$ final states

4.1 Analysis of $\chi_{cJ} \to p\bar{p}K^+K^-$

4.1.1 Final event selection

In this section, our description mainly focuses on χ_{c0}, because procedures of analysis for three states χ_{cJ} are similar.

In order to choose the proper χ^2_{4c} requirement, we use the figure of merit (FOM) [17] to optimize this requirement. The χ^2_{4c} cut is determined by optimizing the value of $S/\sqrt{S+B}$ (FOM) and the optimized curve of χ^2_{4c} is also shown in Fig. 1, where S refers to MC signal sample of $\chi_{c0} \to p\bar{p}K^+K^-$ decay mode and $S+B$ is that number of events candidate of data within $3.365\ \mathrm{GeV}/c^2 < M(p\bar{p}K^+K^-) < 3.455\ \mathrm{GeV}/c^2$ for χ_{c0}. The χ^2_{4c} is required to be less than 40 as indicated in that figure.

To reject possible backgrounds with two photons in the final states, events with the χ^2_{4c} value for the signal hypothesis should be less than those for the background hypotheses $\chi^2_{\gamma\gamma K^+K^-p\bar{p}}$.

The distributions of invariant mass of pK^-, $\bar{p}K^+$ and K^+K^- within χ_{c0} mass region are shown in Fig. 2, where clusters of events corresponding to possible backgrounds with $\Lambda(1520)$, $\bar{\Lambda}(1520)$ and ϕ production are evident. To suppress backgrounds containing $\Lambda(1520)$, $\bar{\Lambda}(1520)$ or ϕ, the requirements $|M(pK^-) - m(\Lambda(1520))| > 0.03\ \mathrm{GeV}/c^2$, $|M(\bar{p}K^+) - m(\bar{\Lambda}(1520))| > 0.03\ \mathrm{GeV}/c^2$ and $|M(K^+K^-) - m(\phi)| > 0.01\ \mathrm{GeV}/c^2$ are applied, where $m(\Lambda(1520))$, $m(\bar{\Lambda}(1520))$ and $m(\phi)$ are the nominal masses of $\Lambda(1520)$, $\bar{\Lambda}(1520)$ and ϕ, respectively.

All the final selection criteria are listed here:

- $\chi^2_{4c} < 40$
- $\chi^2_{4c} < \chi^2_{\gamma\gamma K^+K^-p\bar{p}}$
- $|M(pK^-) - m(\Lambda(1520))| > 0.03\ \mathrm{GeV}/c^2$

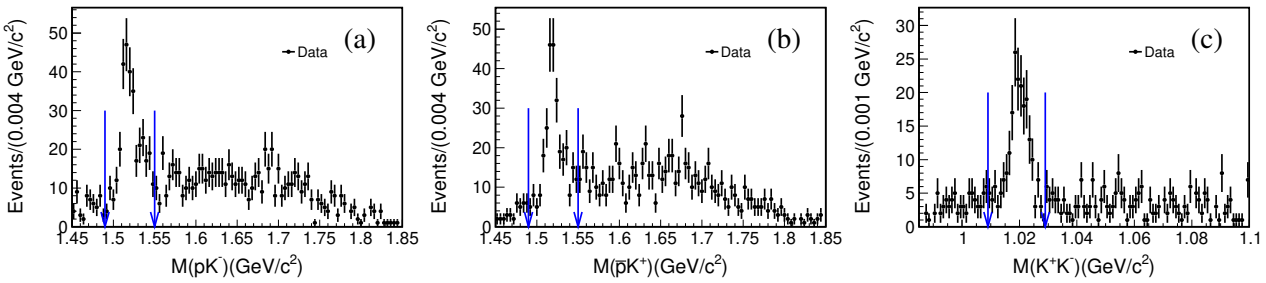

Figure 2: (a) Veto of $\Lambda(1520)$; (b)Veto of $\bar{\Lambda}(1520)$; (C)Veto of ϕ. The dots with error bars are data.

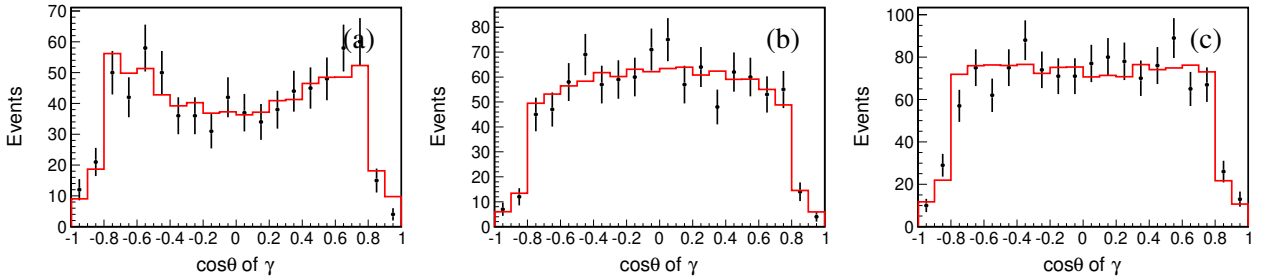

Figure 3: The cosθ distribution of γ in center-of-mass frame. (a) χ_{c0} (b) χ_{c1} (c)χ_{c2}. The dots with error bars are data., the red histograms represent the signal MC of χ_{cJ} $(J = 0, 1, 2)$.

- $|M(\bar{p}K^+) - m(\bar{\Lambda}(1520))|> 0.03$ GeV/c^2
- $|M(K^+K^-) - m(\phi)|> 0.01$ GeV/c^2

Besides, the cosθ distribution of γ within 3.365 GeV/c^2 $< M(p\bar{p}K^+K^-) <$ 3.455 GeV/c^2 for χ_{c0}, 3.490 GeV/c^2 $<M(p\bar{p}K^+K^-) < 3.530$ GeV/c^2 for χ_{c1}, and 3.530 GeV/c^2 $<M(p\bar{p}K^+K^-) < 3.580$ GeV/c^2 for χ_{c2} are showed in Fig. 3, which indicate that the generated MC events could provide a good description of data.

4.1.2 Background study and fitting result

After applying the previously mentioned selection criteria, the invariant mass distribution of $p\bar{p}K^+K^-$ is displayed in Fig. 4 and the topology analysis of inclusive MC in $\chi_{cJ} \to p\bar{p}K^+K^-$ process is listed in Table 1. From the picture and table, we can see clear χ_{c0}, χ_{c1} and χ_{c2} signals events with low backgrounds. The number of signal events can be obtained by fitting the invariant mass spectrum of $p\bar{p}K^+K^-$. The observed invariant mass spectrum of $p\bar{p}K^+K^-$ is fitted by a function of Breit-Wigner convolved with Gaussian function for signal shape and a second order Chebychev polynomial function for background shape, the natural width of Breit-Wigner function is fixed on the PDG [5] and other parameters are free.

Table 1: The topology of inclusive MC in $\chi_{cJ} \to p\bar{p}K^+K^-$ process.

rowNo	decay tree (decay initial-final states)	iDcyTr	iDcyIFSts	nEtr	nCEtr
1	$\psi' \to \chi_{c2}\gamma, \chi_{c2} \to K^+K^-p\bar{p}$ $(\psi' \dashrightarrow K^+K^-p\bar{p}\gamma)$	1	0	1293	1293
2	$\psi' \to \chi_{c1}\gamma, \chi_{c1} \to K^+K^-p\bar{p}$ $(\psi' \dashrightarrow K^+K^-p\bar{p}\gamma)$	2	0	933	2226
3	$\psi' \to \chi_{c0}\gamma, \chi_{c0} \to K^+K^-p\bar{p}$ $(\psi' \dashrightarrow K^+K^-p\bar{p}\gamma)$	0	0	619	2845
4	$\psi' \to \chi_{c0}\gamma, \chi_{c0} \to K^-p\bar{\Lambda}(1520)^0, \bar{\Lambda}(1520)^0 \to K^+\bar{p}$ $(\psi' \dashrightarrow K^+K^-p\bar{p}\gamma)$	5	0	36	2881
5	$\psi' \to \chi_{c2}\gamma, \chi_{c2} \to K^+\bar{p}\Lambda(1520)^0, \Lambda(1520)^0 \to K^-p$ $(\psi' \dashrightarrow K^+K^-p\bar{p}\gamma)$	4	0	35	2916
6	$\psi' \to \chi_{c0}\gamma, \chi_{c0} \to K^+\bar{p}\Lambda(1520)^0, \Lambda(1520)^0 \to K^-p$ $(\psi' \dashrightarrow K^+K^-p\bar{p}\gamma)$	8	0	34	2950
7	$\psi' \to \chi_{c2}\gamma, \chi_{c2} \to K^-p\bar{\Lambda}(1520)^0, \bar{\Lambda}(1520)^0 \to K^+\bar{p}$ $(\psi' \dashrightarrow K^+K^-p\bar{p}\gamma)$	3	0	33	2983
8	$\psi' \to \chi_{c1}\gamma, \chi_{c1} \to K^-p\bar{\Lambda}(1520)^0, \bar{\Lambda}(1520)^0 \to K^+\bar{p}$ $(\psi' \dashrightarrow K^+K^-p\bar{p}\gamma)$	10	0	26	3009
9	$\psi' \to \chi_{c1}\gamma, \chi_{c1} \to K^+\bar{p}\Lambda(1520)^0, \Lambda(1520)^0 \to K^-p$ $(\psi' \dashrightarrow K^+K^-p\bar{p}\gamma)$	7	0	25	3034
10	$\psi' \to \chi_{c0}\gamma, \chi_{c0} \to \phi p\bar{p}, \phi \to K^+K^-$ $(\psi' \dashrightarrow K^+K^-p\bar{p}\gamma)$	13	0	18	3052
11	$\psi' \to \chi_{c2}\gamma, \chi_{c2} \to \phi p\bar{p}, \phi \to K^+K^-$ $(\psi' \dashrightarrow K^+K^-p\bar{p}\gamma)$	9	0	13	3065
12	$\psi' \to \chi_{c1}\gamma, \chi_{c1} \to f_2(1270)p\bar{p}, f_2(1270) \to K^+K^-$ $(\psi' \dashrightarrow K^+K^-p\bar{p}\gamma)$	15	0	13	3078
13	$\psi' \to \chi_{c1}\gamma, \chi_{c1} \to a_2^0p\bar{p}, a_2^0 \to K^+K^-$ $(\psi' \dashrightarrow K^+K^-p\bar{p}\gamma)$	11	0	10	3088
14	$\psi' \to \chi_{c2}\gamma, \chi_{c2} \to f_2(1270)p\bar{p}, f_2(1270) \to K^+K^-$ $(\psi' \dashrightarrow K^+K^-p\bar{p}\gamma)$	19	0	10	3098
15	$\psi' \to \chi_{c2}\gamma, \chi_{c2} \to a_2^0p\bar{p}, a_2^0 \to K^+K^-$ $(\psi' \dashrightarrow K^+K^-p\bar{p}\gamma)$	6	0	9	3107
16	$\psi' \to \chi_{c0}\gamma, \chi_{c0} \to a_2^0p\bar{p}, a_2^0 \to K^+K^-$ $(\psi' \dashrightarrow K^+K^-p\bar{p}\gamma)$	17	0	6	3113
17	$\psi' \to \chi_{c0}\gamma, \chi_{c0} \to \Lambda(1520)^0\bar{\Lambda}(1520)^0, \Lambda(1520)^0 \to K^-p, \bar{\Lambda}(1520)^0 \to K^+\bar{p}$ $(\psi' \dashrightarrow K^+K^-p\bar{p}\gamma)$	12	0	3	3116

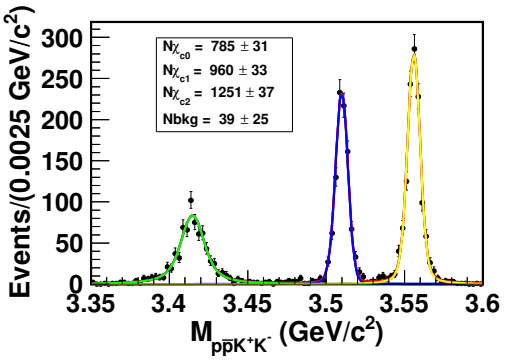

Figure 4: The fitting result of χ_{cJ} $(J = 0, 1, 2)$ on the invariant mass spectrum of $M(p\bar{p}K^+K^-)$. The dots with error bars are data, the green line represents the signal shape of χ_{c0}, the blue line donates the signal shape of χ_{c1}, and the yellow line stands for the signal shape of χ_{c2}.

4.1.3 Branching fraction measurement

The branching fraction of the $\chi_{cJ} \to p\bar{p}K^+K^-$ decay is determined to be

$$B = \frac{N_{obs}}{N_{\psi(2S)} \times B(\psi(2S) \to \gamma\chi_{cJ}) \times \epsilon}, \quad (1)$$

where N_{obs} is the number of observed signal candidates. $N_{\psi(2S)}$ is total number of $\psi(2S)$ events. $B(\psi(2S) \to \gamma\chi_{cJ})$ is branching fractions of $\psi(2S) \to \gamma\chi_{cJ}$ quoted from PDG [5]. ϵ represents detection efficiency of $\psi(2S) \to \gamma\chi_{cJ} \to \gamma p\bar{p}K^+K^-$. The results are listed in Table 2.

Table 2: The results of fitting and branching fractions of χ_{cJ}.

Decay mode	N_{sig}	ϵ (%)	B ($\times 10^{-4}$)
$\chi_{c0} \to p\bar{p}K^+K^-$	785 ± 31	10.1	1.77 ± 0.07
$\chi_{c1} \to p\bar{p}K^+K^-$	960 ± 33	14.2	1.55 ± 0.05
$\chi_{c2} \to p\bar{p}K^+K^-$	1251 ± 37	14.8	1.98 ± 0.06

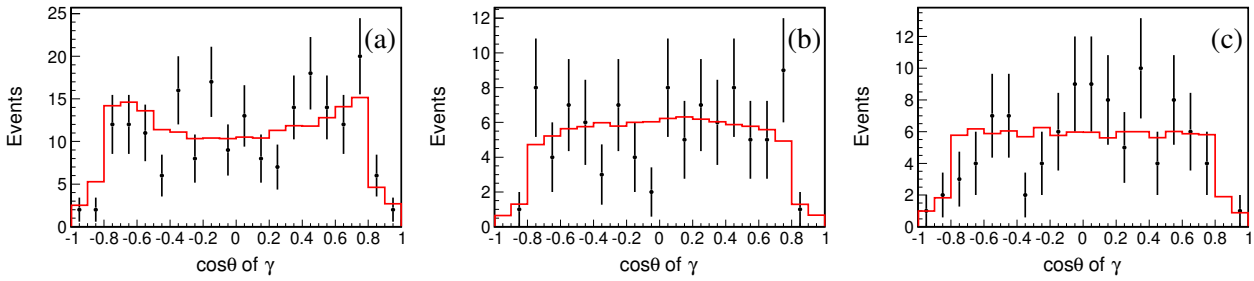

Figure 5: The cosθ distribution of γ in center-of-mass frame. (a) χ_{c0} (b) χ_{c1} (c)χ_{c2}. The dots with error bars are data, the red histograms represent the signal MC of χ_{cJ} $(J = 0, 1, 2)$.

4.2 Analysis of $\chi_{cJ} \to p\bar{p}\phi$

4.2.1 Final event selection

The intermediate states from the χ_{cJ} decaying to $p\bar{p}K^+K^-$ can be studied by configuring the final particles. We investigate the pK^-, $\bar{p}K^+$ configurations as shown in Fig. 2 and veto backgrounds containing $M(pK^-)$ and $M(\bar{p}K^+)$ by applying the same cuts as Sec. 4.1.1. The mass ranges for studying the χ_{cJ} $(J = 0, 1, 2)$ are as follows.

χ_{c0} : 3.365 GeV/c^2 < $M(p\bar{p}K^+K^-)$ < 3.455 GeV/c^2

χ_{c1} : 3.490 GeV/c^2 < $M(p\bar{p}K^+K^-)$ < 3.530 GeV/c^2

χ_{c2} : 3.530 GeV/c^2 < $M(p\bar{p}K^+K^-)$ < 3.580 GeV/c^2

Besides, the cosθ distribution of γ for χ_{cJ} $(J = 0, 1, 2)$ within $|M(K^+K^-) - m(\phi)| < 0.01$ GeV/c^2 are showed in Fig. 5.

4.2.2 Fitting result

To extract the signal yields of $\chi_{cJ} \to p\bar{p}\phi$ decay, we perform the fits to $M(K^+K^-)$, and the fitting results are presented in Fig. 6 for χ_{cJ} $(J = 0, 1, 2)$, respectively. In the fits, $M(K^+K^-)$ is described by a Breit-Wigner function, due to the statistical limitation for χ_{c1} and χ_{c2} decays the natural width is fixed to PDG value [5], while is free for χ_{c0} decay process, and the mass in Breit-Wigner is free for all processes. For backgrounds the third-order MyArgus function is used due to near the threshold. The MyArgus function is defined as

$$f(x) = (x^2/m_0^2 - 1.0)^p \cdot \exp(c(x^2/m_0^2 - 1.0)), \tag{2}$$

where c and p are free parameters and m_0 is a threshold parameter.

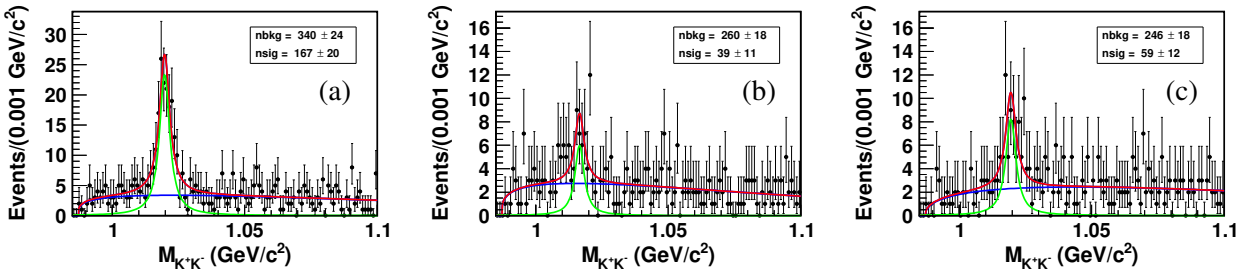

Figure 6: The distributions of $M(K^+K^-)$ in the decays of (a) χ_{c0}, (b) χ_{c1} and (c) χ_{c2}. The dots with error bars are data, the green lines represent the fitting result of signal shape and the blue lines denote the background shape.

4.2.3 Branching fraction measurement

The branching fraction of the $\chi_{cJ} \to p\bar{p}\phi$ decay is determined to be

$$B = \frac{N_{obs}}{N_{\psi(2S)} \times B(\psi(2S) \to \gamma\chi_{cJ}) \times B(\phi \to K^+K^-) \times \epsilon}, \tag{3}$$

where, N_{obs} is the number of observed signal candidates. $N_{\psi(2S)}$ stands for the total number of ψ events. $B(\psi(2S) \to \gamma\chi_{cJ})$ and $B(\phi \to K^+K^-)$ are quoted from PDG [5]. ϵ is the detection efficiency of $\psi(2S) \to \gamma\chi_{cJ} \to \gamma p\bar{p}\phi \to \gamma p\bar{p}K^+K^-$. The results are listed in Table 3. Since the signal of ϕ in χ_{c1} decay is evident with a significance of 3.6σ, the upper limit is also considered and the result is described in Sec. 6.

Table 3: The results of fitting and branching fractions of χ_{cJ}.

Decay mode	N_{sig}	ϵ (%)	B ($\times 10^{-5}$)
$\chi_{c0} \to p\bar{p}\phi$	167 ± 20	11.5	6.72 ± 0.80
$\chi_{c1} \to p\bar{p}\phi$	39 ± 11	16.2	1.11 ± 0.30
$\chi_{c2} \to p\bar{p}\phi$	59 ± 12	16.5	1.69 ± 0.35

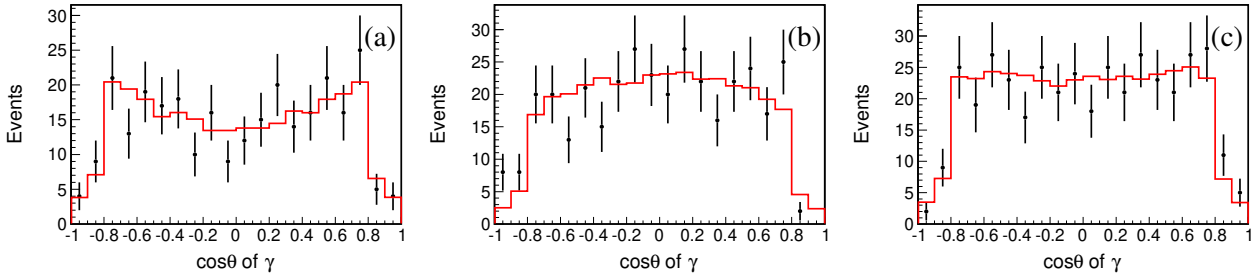

Figure 7: The cosθ distribution of γ in center-of-mass frame. (a) χ_{c0} (b) χ_{c1} (c)χ_{c2}. The dots with error bars are data, the red histograms represent the signal MC of χ_{cJ} ($J = 0, 1, 2$).

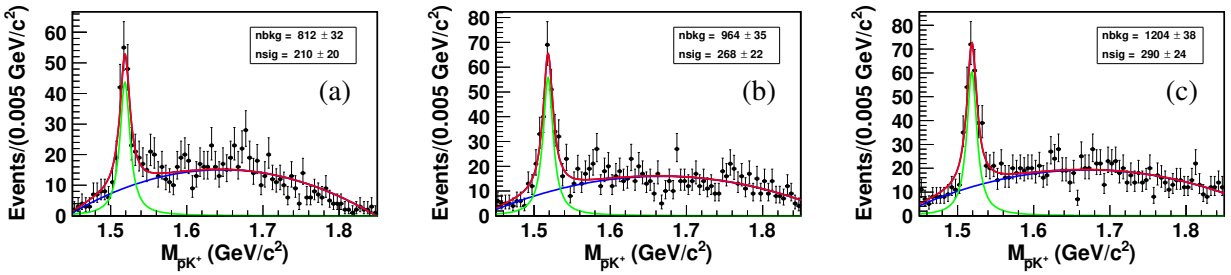

Figure 8: The fit result of $\bar{\Lambda}(1520)$ on the invariant mass spectrum of $M(\bar{p}K^+)$ in the decays of (a) χ_{c0}, (b) χ_{c1} and (c) χ_{c2}. The dots with error bars are data, the green lines represent the fitting result of signal shape and the blue lines denote the background shape.

4.3 Analysis of $\chi_{cJ} \to pK^-\bar{\Lambda}(1520)$

4.3.1 Final event selection

In order to suppress the backgrounds containing $\Lambda(1520)$ and ϕ, the criteria $|M(pK^-) - m(\Lambda(1520))|>$ 0.03 GeV/c^2 and $|M(K^+K^-) - m(\phi)|>$ 0.01 GeV/c^2 are required. The invariant mass distribution $M(\bar{p}K^+)$ is presented in Fig. 8 for $\chi_{cJ}(J = 0, 1, 2)$, respectively. $\bar{\Lambda}(1520)$ signal events are observed clearly.

Besides, the cosθ distribution of γ for χ_{cJ} ($J = 0, 1, 2$) within $|M(\bar{p}K^+) - m(\bar{\Lambda}(1520))|<$ 0.03 GeV/c^2 are showed in Fig. 7.

4.3.2 Fitting result

The invariant mass distribution of $M(\bar{p}K^+)$ is fitted by a Breit-Wigner function, plus a second order Chebychev polynomial for the background. This is shown in Fig. 8. The natural width in Breit-Wigner is fixed according to PDG [5] and the mass in Breit-Wigner is free. The parameters of the second order Chebychev polynomial are also free.

4.3.3 Branching fraction measurement

The branching fraction of the $\chi_{cJ} \to pK^-\bar{\Lambda}(1520)$ decay is determined to be

$$B = \frac{N_{obs}}{N_{\psi(2S)} \times B(\psi(2S) \to \gamma\chi_{cJ}) \times B(\bar{\Lambda}(1520) \to \bar{p}K^+) \times \epsilon}, \quad (4)$$

where, N_{obs} is the number of observed signal candidates. $N_{\psi(2S)}$ stands for the total number of ψ events. $B(\psi(2S) \to \gamma\chi_{cJ})$ and $B(\bar{\Lambda}(1520) \to \bar{p}K^+)$ are quoted from PDG [5]. ϵ is the detection efficiency of $\psi \to \gamma\chi_{cJ} \to \gamma pK^-\bar{\Lambda}(1520) \to \gamma p\bar{p}K^+K^-$.The results are listed in Table 4.

Table 4: The results of fitting and branching fractions of χ_{cJ}.

Decay mode	N_{sig}	ϵ (%)	B ($\times 10^{-4}$)
$\chi_{c0} \to pK^-\bar{\Lambda}(1520)$	210 ± 20	12.4	1.71 ± 0.16
$\chi_{c1} \to pK^-\bar{\Lambda}(1520)$	268 ± 22	16.8	1.63 ± 0.14
$\chi_{c2} \to pK^-\bar{\Lambda}(1520)$	290 ± 24	16.8	1.80 ± 0.15

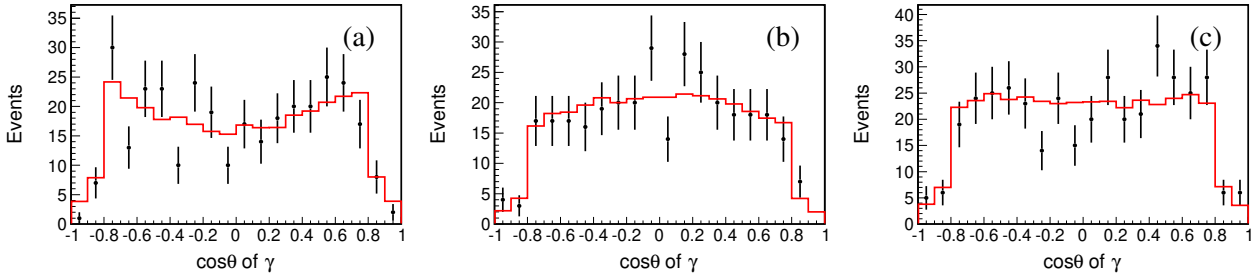

Figure 9: The cosθ distribution of γ in center-of-mass frame. (a) χ_{c0} (b) χ_{c1} (c)χ_{c2}. The dots with error bars are data, the red histograms represent the signal MC of χ_{cJ} ($J = 0, 1, 2$).

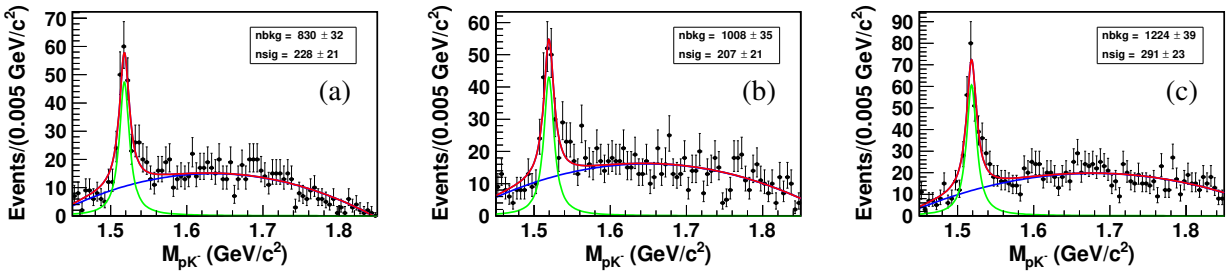

Figure 10: The fitting result of $\Lambda(1520)$ on the invariant mass spectrum of $M(pK^-)$ in the decays of (a) χ_{c0}, (b) χ_{c1} and (c) χ_{c2}. The dots with error bars are data, the green lines represent the fitting result of signal shape and the blue lines denote the background shape.

4.4 Analysis of $\chi_{cJ} \to \Lambda(1520)\bar{p}K^+$

4.4.1 Final event selection

In order to suppress the backgrounds containing $\bar{\Lambda}(1520)$ and ϕ, the criteria $|M(\bar{p}K^+) - m(\bar{\Lambda}(1520))|>$ 0.03 GeV/c^2 and $|M(K^+K^-) - m(\phi)|>$ 0.01 GeV/c^2 are required. The invariant mass distribution $M(pK^-)$ is presented in Fig. 10 for $\chi_{cJ}(J = 0, 1, 2)$, respectively. $\Lambda(1520)$ signal events are observed clearly.

Besides, the cosθ distribution of γ for χ_{cJ} ($J = 0, 1, 2$) within $|M(pK^-) - m(\Lambda(1520))|< 0.03$ GeV/c^2 are showed in Fig. 9.

4.4.2 Fitting result

The invariant mass distribution of $M(pK^-)$ is fitted by a Breit-Wigner function, plus a second order Chebychev polynomial for the background. This is shown in Fig. 10. The natural width in Breit-Wigner is fixed according to PDG [5] and the mass in Breit-Wigner is free. The parameters of the second order Chebychev polynomial are also free.

4.4.3 Branching fraction measurement

The branching fraction of the $\chi_{cJ} \to \Lambda(1520)\bar{p}K^+$ decay is determined to be

$$B = \frac{N_{obs}}{N_{\psi(2S)} \times B(\psi(2S) \to \gamma\chi_{cJ}) \times B(\Lambda(1520) \to pK^-) \times \epsilon}, \tag{5}$$

where, N_{obs} is the number of observed signal candidates. $N_{\psi(2S)}$ stands for the total number of ψ events. $B(\psi(2S) \to \gamma\chi_{cJ})$ and $B(\Lambda(1520) \to pK^-)$ are quoted from PDG [5]. ϵ is the detection efficiency of $\psi \to \gamma\chi_{cJ} \to \gamma\bar{p}K^+\Lambda(1520) \to \gamma p\bar{p}K^+K^-$. The results are listed in Table 5.

Table 5: The results of fitting and branching fractions of χ_{cJ}.

Decay mode	N_{sig}	ϵ (%)	B ($\times 10^{-4}$)
$\chi_{c0} \to \Lambda(1520)\bar{p}K^+$	228 ± 21	12.6	1.83 ± 0.17
$\chi_{c1} \to \Lambda(1520)\bar{p}K^+$	207 ± 21	16.9	1.24 ± 0.13
$\chi_{c2} \to \Lambda(1520)\bar{p}K^+$	291 ± 23	16.9	1.79 ± 0.14

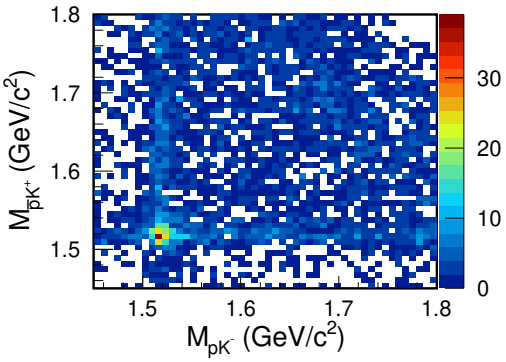

Figure 11: The scatter plot of $M(pK^-)$ versus $M(\bar{p}K^+)$ in the decays of χ_{cJ} $(J = 0, 1, 2)$.

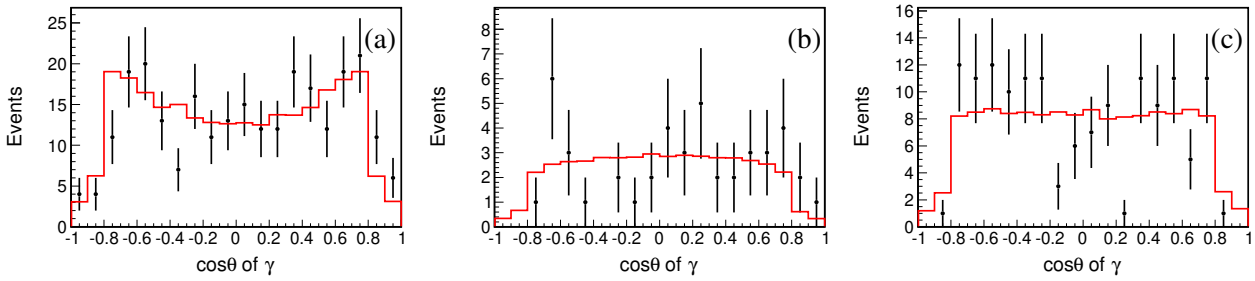

Figure 12: The cosθ distribution of γ in center-of-mass frame. (a) χ_{c0} (b) χ_{c1} (c)χ_{c2}. The dots with error bars are data, the red histograms represent the signal MC of χ_{cJ} $(J = 0, 1, 2)$.

4.5 Analysis of $\chi_{cJ} \to \Lambda(1520)\bar{\Lambda}(1520)$

4.5.1 Final event selection

In Fig. 11, clear enhancement around 1.52 GeV/c^2 indicates the existence of $\chi_{cJ} \to \Lambda(1520)\bar{\Lambda}(1520)$. Events are selected as signals that ϕ has been rejected by the criterion $|M(K^+K^-) - m(\phi)|> 0.01$ GeV/c^2 , and a 2-Dimensional fit is used to estimate the signal and the background.

Besides, the cosθ distribution of γ for χ_{cJ} $(J = 0, 1, 2)$ within $|M(pK^-) - m(\Lambda(1520))|< 0.03$ GeV/c^2 and $|M(\bar{p}K^+) - m(\bar{\Lambda}(1520))|< 0.03$ GeV/c^2 are showed in Fig. 12, which indicate that the generated MC events could provide a good description of data.

4.5.2 Fitting result

An unbinned likelihood fit is performed to obtain the signal and background's yields and the 2-dimension fit is applied. In the fit, A composite PDF is constructed as follow:

$$F = N_{sig} \times F_{sig} + N_{bkg} \times F_{bkg} + N_{bkg1} \times F_{bkg1} + N_{bkg2} \times F_{bkg2}, \quad (6)$$

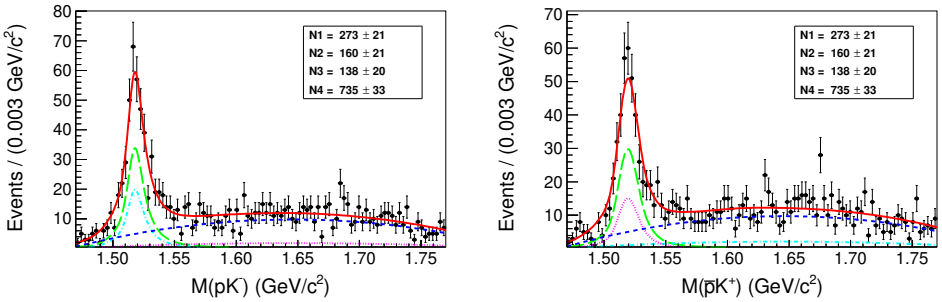

Figure 13: The 2-dimension fitting result for χ_{c0}. The dots with error bars are data, the left plot is the projection of $M(pK^-)$, the right plot is the projection of $M(\bar{p}K^+)$, the green line is used to describe the shape of signal, the blue line is the shape of non-peaking background, the light blue line is the shape of background with $\Lambda(1520)$, the pink line is the shape of background with $\bar{\Lambda}(1520)$.

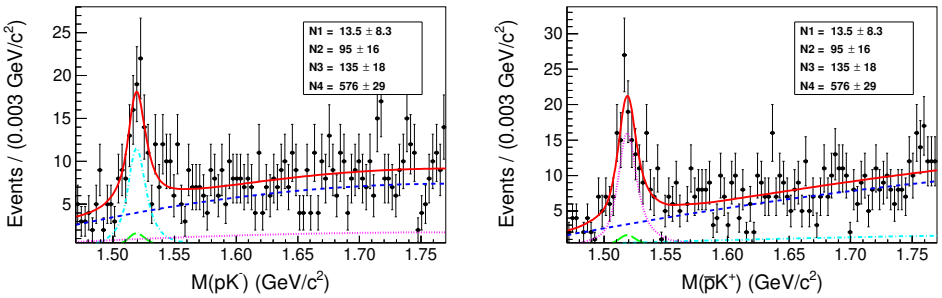

Figure 14: The 2-dimension fitting result for χ_{c1}. The dots with error bars are data, the left plot is the projection of $M(pK^-)$, the right plot is the projection of $M(\bar{p}K^+)$, the green line is used to describe the shape of signal, the blue line is the shape of non-peaking background, the light blue line is the shape of background with $\Lambda(1520)$, the pink line is the shape of background with $\bar{\Lambda}(1520)$.

where, N_{sig} is the observed number of signal events, N_{bkg} is the observed number of background events, F_{sig} and F_{bkg}, F_{bkg1}, F_{bkg2} are signal PDF and background PDF, respectively.

The 2-dimensional signal and background PDFs are constructed by simply multiplying two 1-dimensional PDFs, respectively,

$$\begin{aligned} F_{sig} &= PDF_{sig}(M(pK^-)) \times PDF_{sig}(M(\bar{p}K^+)), \\ F_{bkg} &= PDF_{bkg}(M(pK^-)) \times PDF_{bkg}(M(\bar{p}K^+)), \\ F_{bkg1} &= PDF_{sig}(M(pK^-)) \times PDF_{bkg}(M(\bar{p}K^+)), \\ F_{bkg2} &= PDF_{bkg}(M(pK^-)) \times PDF_{sig}(M(\bar{p}K^+)), \end{aligned} \tag{7}$$

where, $PDF_{sig}(M(pK^-))$ and $PDF_{sig}(M(\bar{p}K^+))$ are the distribution of PDF shape obtained from the MC simulation, respectively. $PDF_{bkg}(M(pK^-))$ and $PDF_{bkg}(M(\bar{p}K^+))$ are the PDF of background represented by the second-order Chebychev Polynominal function with the free parameters. The fitting results are shown in Fig. 13, Fig. 14 and Fig. 15, respectively.

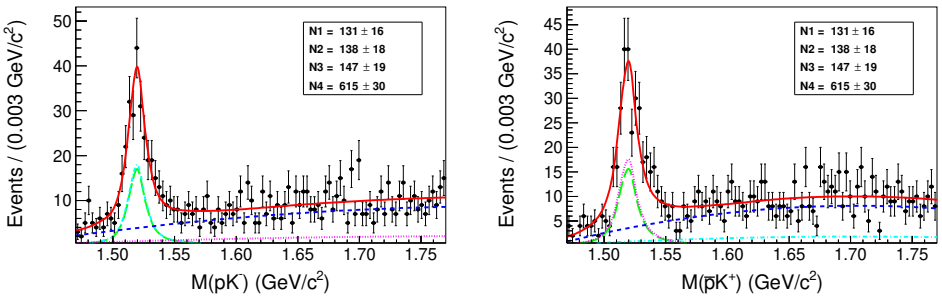

Figure 15: The 2-dimension fitting result for χ_{c2}. The dots with error bars are data,the left plot is the projection of $M(pK^-)$, the right plot is the projection of $M(\bar{p}K^+)$, the green line is used to describe the shape of signal, the blue line is the shape of non-peaking background, the light blue line is the shape of background with $\Lambda(1520)$, the pink line is the shape of background with $\bar{\Lambda}(1520)$.

4.5.3 Branching fraction measurement

The branching fraction of the $\chi_{cJ} \to \Lambda(1520)\bar{\Lambda}(1520)$ decay is determined to be

$$B = \frac{N_{obs}}{N_{\psi(2S)} \times B\,(\psi(2S) \to \gamma\chi_{cJ}) \times B(\Lambda(1520) \to pK)^2 \times \epsilon} \tag{8}$$

where, N_{obs} is the number of observed signal candidates. $N_{\psi(2S)}$ stands for the total number of $\psi(2S)$ events. $B(\psi(2S) \to \gamma\chi_{cJ})$, $B(\bar{\Lambda}(1520) \to \bar{p}K^+)$ and $B(\Lambda(1520) \to pK^-)$ are quoted from PDG [5]. ϵ is the detection efficiency of $\psi \to \gamma\chi_{cJ} \to \gamma\Lambda(1520)\bar{\Lambda}(1520) \to \gamma p\bar{p}K^+K^-$. The results are listed in Table 6. Since the significance can be calculated to be 1.8σ for the $\chi_{c1} \to \Lambda(1520)\bar{\Lambda}(1520)$ decay, the upper limit is considered and the result is described in Sec. 6.

Table 6: The results of fitting and branching fractions of χ_{cJ}.

Decay mode	N_{sig}	ϵ (%)	B ($\times 10^{-4}$)
$\chi_{c0} \to \Lambda(1520)\bar{\Lambda}(1520)$	273 ± 21	16.8	7.33 ± 0.56
$\chi_{c2} \to \Lambda(1520)\bar{\Lambda}(1520)$	131 ± 16	22.7	2.68 ± 0.33

5 Systematic Uncertainty

5.1 MDC track and PID

The MDC tracking efficiencies of charged protons and kaons are investigated using nearly background-free(clean) control samples of $J/\psi \to p\bar{p}\pi^+\pi^-$ and $J/\psi \to K^0_S K^\pm\pi^\mp$ [18,19], respectively. The difference in tracking efficiencies between MC and data is 1% for each charged proton and koan. In our work, there are four charged tracks of kaon and proton, so the systematic uncertainties from tracking is 4%. We have use the particle identification to identify the kaon and proton, the uncertainty of PID is 1% per track, so the uncertainty from this item is 4%.

5.2 Photon selection

The photon detection efficiency has been studied using a control sample of $J/\psi \to \rho^0\pi^0$ [20]. The results indicate that the difference between the detection efficiencies of data and MC is around 1% per photon. Thus, 1% is taken as the total systematic uncertainty for the detection of one photon in this analysis.

5.3 The number of $\psi(2S)$

The systematic uncertainty due to the number of $\psi(2S)$ events is determined to be 0.6% according to Ref. [21].

5.4 Branching fraction of intermediate state

The systematic uncertainty due to branching fraction of intermediate states are from PDG [5], there are 2.0% for $\psi(2S) \to \gamma\chi_{cJ}$ decay, 1.0% for $\phi \to K^+K^-$ decay and 2.0% for $\Lambda(1520) \to pK^-$.

5.5 The 4C kinematic fit

The systematic uncertainty due to 4C kinematic fit is estimated by correcting helix parameters of charged tracks described in Ref. [22], the efficiency differences of signal MC before and after correction are considered as the systematic uncertainties. Fig. 16 gives the comparison with and without tracking helix correction using χ^2 test for the decay mode $\chi_{c0} \to p\bar{p}K^+K^-$. The systematic uncertainties from the 4C kinematic fit are listed in the following Table 7.

5.6 Fitting range

The uncertainty from fitting range is estimated by varying the fitting range. The resulting largest differences of all decay modes are treated as the systematic uncertainties listed in Table 8.

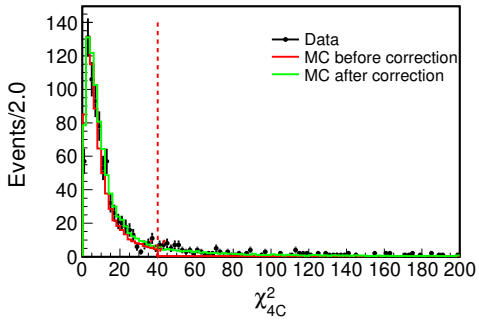

Figure 16: The decay mode $\chi_{c0} \to p\bar{p}K^+K^-$ of χ^2_{4C} distribution between track correction results and nominal results. Dots with error bars are experimental data, the red line denotes MC sample before track correction, the green line denotes the MC sample after track correction.

Table 7: The systematic uncertainty from the 4C kinematic fit.(%)

Decay mode	χ_{c0}	χ_{c1}	χ_{c2}
$\chi_{cJ} \to p\bar{p}K^+K^-$	0.7	0.1	0.4
$\chi_{cJ} \to p\bar{p}\phi$	0.7	0.8	0.8
$\chi_{cJ} \to pK^-\bar{\Lambda}(1520)$	0.8	0.8	1.0
$\chi_{cJ} \to \Lambda(1520)\bar{p}K^+$	0.9	0.9	0.9
$\chi_{cJ} \to \Lambda(1520)\bar{\Lambda}(1520)$	0.6	0.7	0.6

Table 8: The systematic uncertainty from fitting range.(%)

Decay mode	Change (GeV/c^2)	χ_{c0}	χ_{c1}	χ_{c2}
$\chi_{cJ} \to p\bar{p}K^+K^-$	[3.351,3.599] / [3.345,3.605]	0.9	3.2	1.0
$\chi_{cJ} \to p\bar{p}\phi$	[0.985,1.09] / [0.985,1.11]	1.6	0.3	4.0
$\chi_{cJ} \to pK^-\bar{\Lambda}(1520)$	[1.46,1.84] / [1.44,1.86]	1.4	2.6	3.5
$\chi_{cJ} \to \Lambda(1520)\bar{p}K^+$	[1.46,1.84] / [1.44,1.86]	3.4	5.5	2.7
$\chi_{cJ} \to \Lambda(1520)\bar{\Lambda}(1520)$	[1.48,1.76] / [1.46,1.78]	3.6	17.0	5.9

5.7 Signal shape

In order to estimate the systematic uncertainty due to the difference of different signal shape, alternative fits are performed to determine the yields of signal events, replacing original shape with the other function. The branching fraction differences are taken as the systematic uncertainties, and the values are listed in Table 9.

Table 9: The systematic uncertainty from the signal shape.(%)

Decay mode	Change	χ_{c0}	χ_{c1}	χ_{c2}
$\chi_{cJ} \to p\bar{p}K^+K^-$	MC shape	8.5	1.3	2.7
$\chi_{cJ} \to p\bar{p}\phi$	MC shape	1.6	12.1	3.5
$\chi_{cJ} \to pK^-\bar{\Lambda}(1520)$	MC shape	3.6	0.0	0.4
$\chi_{cJ} \to \Lambda(1520)\bar{p}K^+$	MC shape	5.1	1.9	0.6
$\chi_{cJ} \to \Lambda(1520)\bar{\Lambda}(1520)$	a Breit-Wigner function	7.3	20.4	9.9

5.8 Background shape

To estimate the systematic uncertainty from background shape, we perform a alternative fit by changing original function to other function, and the differences of branching fraction are taken as the uncertainties and the details can be found in Table 10.

Table 10: The systematic uncertainty from the background shape.(%)

Decay mode	Change	χ_{c0}	χ_{c1}	χ_{c2}
$\chi_{cJ} \to p\bar{p}K^+K^-$	1st Polynomial function	0.8	0.3	0.6
$\chi_{cJ} \to p\bar{p}\phi$	3rd Chebychev Polynomial function	1.9	19.9	3.4
$\chi_{cJ} \to pK^-\bar{\Lambda}(1520)$	3rd Chebychev Polynomial function	9.5	1.0	2.6
$\chi_{cJ} \to \Lambda(1520)\bar{p}K^+$	3rd Chebychev Polynomial function	4.1	2.2	0.2
$\chi_{cJ} \to \Lambda(1520)\bar{\Lambda}(1520)$	3rd Polynomial function	1.1	1.6	0.5

5.9 The mass window requirement

To estimate the systematic uncertainty of the veto of invariant mass, we change the cut value for data and MC by enlarging and narrowing the mass window range, then perform the same fit with nominal analysis. The maximum resulting differences of branching fractions are regarded as the systematic uncertainties for each requirement. The values are shown in Table 11.

5.10 Total systematic uncertainty

The summaries of systematic uncertainty are listed in Table 12, Table 13, Table 14, Table 15 and Table 16 for above decay modes, respectively. The total systematic uncertainties are the square root of quadratic sum of each item.

Table 11: The systematic uncertainty from veto of all decay modes.(%)

Decay mode	Mass window	Change(MeV)	χ_{c0}	χ_{c1}	χ_{c2}
$\chi_{cJ} \to p\bar{p}K^+K^-$	$M(pK^-)$	±5	1.8	0.1	1.0
	$M(\bar{p}K^+)$	±5	1.4	2.3	2.1
	$M(K^+K^-)$	±2	1.9	1.4	0.9
$\chi_{cJ} \to p\bar{p}\phi$	$M(pK^-)M(\bar{p}K^+)$	±5	2.9	5.1	4.6
$\chi_{cJ} \to pK^-\bar{\Lambda}(1520)$	$M(pK^-)$	±5	2.2	1.1	1.5
	$M(K^+K^-)$	±2	0.8	0.6	0.5
$\chi_{cJ} \to \Lambda(1520)\bar{p}K^+$	$M(\bar{p}K^+)$	±5	1.8	2.3	0.4
	$M(K^+K^-)$	±2	1.7	1.2	0.9
$\chi_{cJ} \to \Lambda(1520)\bar{\Lambda}(1520)$	$M(K^+K^-)$	±2	0.3	0.1	0.4

Table 12: Systematic uncertainties on the branching fraction measurement for $\chi_{cJ} \to p\bar{p}K^+K^-$ (%).

Source	$\chi_{c0} \to p\bar{p}K^+K^-$	$\chi_{c1} \to p\bar{p}K^+K^-$	$\chi_{c2} \to p\bar{p}K^+K^-$
MDC track	4.0	4.0	4.0
PID	4.0	4.0	4.0
Photon selection	1.0	1.0	1.0
Total Number of $\psi(2S)$	0.6	0.6	0.6
The 4C Kinematic Fit	0.7	0.1	0.4
Intermediate Decay	2.0	2.0	2.0
Signal shape	8.5	1.3	2.7
Background shape	0.8	0.3	0.6
Fitting range	0.9	3.2	1.0
Veto of $\Lambda(1520)$	1.8	0.1	1.0
Veto of $\bar{\Lambda}(1520)$	1.4	2.3	2.1
Veto of ϕ	1.9	1.4	0.9
Total	11.0	7.5	7.2

Table 13: Systematic uncertainties on the branching fraction measurement for $\chi_{cJ} \to p\bar{p}\phi$ (%).

Source	$\chi_{c0} \to p\bar{p}\phi$	$\chi_{c1} \to p\bar{p}\phi$	$\chi_{c2} \to p\bar{p}\phi$
MDC track	4.0	4.0	4.0
PID	4.0	4.0	4.0
Photon selection	1.0	1.0	1.0
Total Number of $\psi(2S)$	0.6	0.6	0.6
The 4C Kinematic Fit	0.7	0.8	0.8
Intermediate Decay	2.2	2.2	2.2
Signal shape	1.6	12.1	3.5
Background shape	1.9	19.9	3.4
Fitting range	1.6	0.3	4.0
Veto of $\Lambda(1520)/\bar{\Lambda}(1520)$	2.9	5.1	4.6
Total	7.5	24.6	10.0

Table 14: Systematic uncertainties on the branching fraction measurement for $\chi_{cJ} \to pK^-\bar{\Lambda}(1520)$ (%).

Source	$\chi_{c0} \to pK^-\bar{\Lambda}(1520)$	$\chi_{c1} \to pK^-\bar{\Lambda}(1520)$	$\chi_{c2} \to pK^-\bar{\Lambda}(1520)$
MDC track	4.0	4.0	4.0
PID	4.0	4.0	4.0
Photon selection	1.0	1.0	1.0
Total Number of $\psi(2S)$	0.6	0.6	0.6
The 4C Kinematic Fit	0.8	0.8	1.0
Intermediate Decay	2.0	2.0	2.0
Signal shape	3.6	0.1	0.4
Background shape	9.5	1.0	2.6
Fitting range	1.4	2.6	3.5
Veto of $\Lambda(1520)$	2.2	1.1	1.5
Veto of ϕ	0.8	0.6	0.5
Total	12.2	6.9	7.7

Table 15: Systematic uncertainties on the branching fraction measurement for $\chi_{cJ} \to \Lambda(1520)\bar{p}K^+$ (%).

Source	$\chi_{c0} \to \Lambda(1520)\bar{p}K^+$	$\chi_{c1} \to \Lambda(1520)\bar{p}K^+$	$\chi_{c2} \to \Lambda(1520)\bar{p}K^+$
MDC track	4.0	4.0	4.0
PID	4.0	4.0	4.0
Photon selection	1.0	1.0	1.0
Total Number of $\psi(2S)$	0.6	0.6	0.6
The 4C Kinematic Fit	0.9	0.9	0.9
Intermediate Decay	2.0	2.0	2.0
Signal shape	5.1	1.9	0.6
Background shape	4.1	2.2	0.2
Fitting range	3.4	5.5	2.7
Veto of $\bar{\Lambda}(1520)$	1.8	2.3	0.4
Veto of ϕ	1.7	1.2	0.9
Total	9.9	9.1	6.8

Table 16: Systematic uncertainties on the branching fraction measurement for $\chi_{cJ} \to \Lambda(1520)\bar{\Lambda}(1520)$ (%).

Source	$\chi_{c0} \to \Lambda(1520)\bar{\Lambda}(1520)$	$\chi_{c1} \to \Lambda(1520)\bar{\Lambda}(1520)$	$\chi_{c2} \to \Lambda(1520)\bar{\Lambda}(1520)$
MDC track	4.0	4.0	4.0
PID	4.0	4.0	4.0
Photon selection	1.0	1.0	1.0
Total Number of $\psi(2S)$	0.6	0.6	0.6
The 4C Kinematic Fit	0.6	0.7	0.6
Intermediate Decay	3.5	3.5	3.5
Signal shape	7.3	20.4	9.9
Background shape	1.1	1.6	0.5
Fitting range	3.6	17.0	5.9
Veto of ϕ	0.3	0.1	0.4
Total	10.7	27.5	13.4

6 Upper limit

To determine the upper limits of the branching fraction on $\chi_{c1} \to p\bar{p}\phi$ and $\chi_{c1} \to \Lambda(1520)\bar{\Lambda}(1520)$, a series of unbinned maximum likelihood fits are performed. In the fits, the fit models of signal and background are the same as their nominal ones, which are described in Sec. 4.2.2 and 4.5.2, respectively, while we fix the mean value of Breit-Wigner function to PDG [5] value for fits of ϕ decay. To incorporate the multiplicative systematic uncertainty in the calculation of the upper limit, the likelihood distribution is smeared via [23, 24]

$$L'(n') \propto \int_0^\infty L(n\frac{\epsilon}{\epsilon_0})\exp[\frac{-(\epsilon-\epsilon_0)^2}{2\sigma_\epsilon^2}]d\epsilon, \tag{9}$$

where $L(n)$ is the likelihood distribution as a function of the yield n, ϵ_0 is the detection efficiency and σ_ϵ is the multiplicative systematic uncertainty. Figure 17 shows the likelihood distributions with and without incorporating the systematic uncertainties. The number limits of the $\chi_{c1} \to p\bar{p}\phi$ and $\chi_{c1} \to \Lambda(1520)\bar{\Lambda}(1520)$ are then determined to be $N_{UL} = 50$ and 35, respectively.

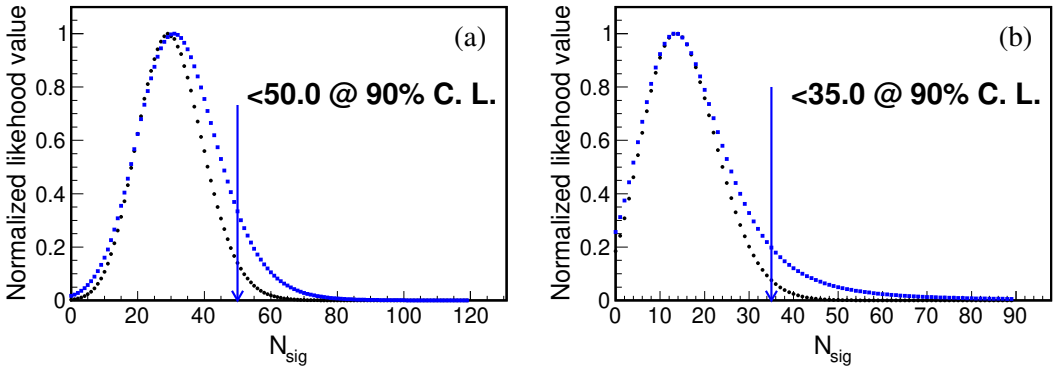

Figure 17: The normalized likelihood distributions with only one additive systematic uncertainty (background shape). (a) $\chi_{c1} \to p\bar{p}\phi$. (b) $\chi_{c1} \to \Lambda(1520)\bar{\Lambda}(1520)$. The black dots are the results with the nominal fits, the blue dots are obtained with incorporating the multiplicative and additive systematic uncertainties. The arrows are the position of the upper limit on the signal yields at 90% confidence level (C. L.).

With the detection efficiency of 16.2% obtained from the MC simulation of $\chi_{c1} \to p\bar{p}\phi$, the upper limits on the branching fraction is calculated with Eq. 10. The results of upper limit of the branching fraction are shown in Table 17.

$$B < \frac{N_{UL}}{N_{\psi(2S)} \times B(\psi(2S) \to \gamma\chi_{cJ}) \times B(\phi \to K^+K^-) \times \epsilon}. \tag{10}$$

With the detection efficiency of 22.4% obtained from the MC simulation of $\chi_{c1} \to \Lambda(1520)\bar{\Lambda}(1520)$, the upper limits on the branching fraction is calculated with Eq. 11. The results of upper limit of the branching fraction are shown in Table 17.

$$B < \frac{N_{UL}}{N_{\psi(2S)} \times B\,(\psi(2S) \to \gamma\chi_{cJ}) \times B(\Lambda(1520) \to pK)^2 \times \epsilon}. \quad (11)$$

Table 17: The results of upper limit of the branching fraction.

Decay mode	N_{UL}	ϵ (%)	Results
$\chi_{c1} \to p\bar{p}\phi$	50	16.2	1.44×10^{-5}
$\chi_{c1} \to \Lambda(1520)\bar{\Lambda}(1520)$	35	22.4	0.71×10^{-4}

7 Summary

Based on 448.1×10^6 events collected from BESIII detector at BEPCII storage ring at center-of-mass energy $\sqrt{s}$ = 3.686 GeV in 2009 and 2012, we study specific hadron decay modes of χ_{cJ} listed in Table 18. The upper limit results of $\chi_{c1} \to p\bar{p}\phi$ and $\chi_{c1} \to \Lambda(1520)\bar{\Lambda}(1520)$ are determined to be $B(\chi_{c1} \to p\bar{p}\phi) < 1.44 \times 10^{-5}$ and $B(\chi_{c1} \to \Lambda(1520)\bar{\Lambda}(1520)) < 0.71 \times 10^{-4}$ at 90% C. L., respectively. For the latter the branching fraction is also measured in the analysis because of the evident result with a significance level of 3.6σ for the decay $\chi_{c1} \to p\bar{p}\phi$. Other hadronic decay modes of χ_{cJ} can be improved considering simple clean environment and excellent detector performance. In this analysis, the branching fractions are consistent with the previous results within 1σ standard deviation in $\chi_{c1}/\chi_{c2} \to p\bar{p}K^+K^-$, $\chi_{c0} \to p\bar{p}\phi$ and $\chi_{c0}/\chi_{c2} \to pK^-\bar{\Lambda}(1520) + c.c.$. The branching fractions are different in some decays. In the $\chi_{c0} \to p\bar{p}K^+K^-$, $\chi_{c2} \to p\bar{p}\phi$, $\chi_{c1} \to pK^-\bar{\Lambda}(1520) + c.c.$ and $\chi_{c2} \to \Lambda(1520)\bar{\Lambda}(1520)$, the differences are covered by 2σ, and in $\chi_{c0} \to \Lambda(1520)\bar{\Lambda}(1520)$ the difference is covered by 3σ. The big difference in $\chi_{c0} \to \Lambda(1520)\bar{\Lambda}(1520)$ may be caused by the difference of method of the signal yields extraction, because the 2-dimension fit is used in this analysis while the sideband method is performed in the previous work.

Table 18: Summary of the measured branching fraction.

Decay mode	This work	Previous measurement [25]
$\chi_{c0} \to p\bar{p}K^+K^-(\times 10^{-4})$	$1.77 \pm 0.07 \pm 0.20$	$1.24 \pm 0.20 \pm 0.18$
$\chi_{c1} \to p\bar{p}K^+K^-(\times 10^{-4})$	$1.55 \pm 0.05 \pm 0.12$	$1.35 \pm 0.15 \pm 0.19$
$\chi_{c2} \to p\bar{p}K^+K^-(\times 10^{-4})$	$1.98 \pm 0.06 \pm 0.14$	$2.08 \pm 0.19 \pm 0.30$
$\chi_{c0} \to p\bar{p}\phi(\times 10^{-5})$	$6.72 \pm 0.80 \pm 0.50$	$6.12 \pm 1.18 \pm 0.86$
$\chi_{c1} \to p\bar{p}\phi(\times 10^{-5})$	$1.11 \pm 0.30 \pm 0.27$ (< 1.44)	< 1.82
$\chi_{c2} \to p\bar{p}\phi(\times 10^{-5})$	$1.69 \pm 0.35 \pm 0.17$	$3.04 \pm 0.85 \pm 0.43$
$\chi_{c0} \to pK^-\bar{\Lambda}(1520)(\times 10^{-4})$	$1.71 \pm 0.16 \pm 0.21$	$3.00 \pm 0.58 \pm 0.50$ (+c.c.)
$\chi_{c1} \to pK^-\bar{\Lambda}(1520)(\times 10^{-4})$	$1.63 \pm 0.14 \pm 0.11$	$1.81 \pm 0.38 \pm 0.28$ (+c.c.)
$\chi_{c2} \to pK^-\bar{\Lambda}(1520)(\times 10^{-4})$	$1.80 \pm 0.15 \pm 0.14$	$3.06 \pm 0.50 \pm 0.54$ (+c.c.)
$\chi_{c0} \to \Lambda(1520)\bar{p}K^+(\times 10^{-4})$	$1.83 \pm 0.17 \pm 0.18$	-
$\chi_{c1} \to \Lambda(1520)\bar{p}K^+(\times 10^{-4})$	$1.24 \pm 0.13 \pm 0.11$	-
$\chi_{c2} \to \Lambda(1520)\bar{p}K^+(\times 10^{-4})$	$1.79 \pm 0.14 \pm 0.12$	-
$\chi_{c0} \to \Lambda(1520)\bar{\Lambda}(1520)(\times 10^{-4})$	$7.33 \pm 0.56 \pm 0.78$	$3.18 \pm 1.11 \pm 0.53$
$\chi_{c1} \to \Lambda(1520)\bar{\Lambda}(1520)(\times 10^{-4})$	< 0.71	< 1.00
$\chi_{c2} \to \Lambda(1520)\bar{\Lambda}(1520)(\times 10^{-4})$	$2.68 \pm 0.33 \pm 0.36$	$5.05 \pm 1.29 \pm 0.93$

References

[1] J. J. Aubert *et al.*, Phys. Rev. Lett. **33**, 1404 (1974).

[2] J. E. Augustin *et al.*, Phys. Rev. Lett. **33**, 1406 (1974).

[3] G. S. Abrams *et al.*, Phys. Rev. Lett. **33**, 1453 (1974).

[4] G. T. Bodwin, E. Braaten, and G. P. Lepage, Phys. Rev. **D 51**, 1125 (1995);
H. W. Huang and K. T. Chao, Phys. Rev. **D 54**, 6850 (1996);
A. Petrelli, Phys. Lett. **B 380**, 159 (1996);
J. Bolz, P. Kroll, and G. A. Schuler, Eur. Phys. J. **C 2**, 705 (1998);
S. H. M. Wong, Eur. Phys. J. **C 14**, 643 (2000).

[5] P. A. Zyla *et al.* (Particle Data Group), Prog. Theor. Exp. Phys. 2020, 083C01 (2020).

[6] M. Ablikim *et al.*(BESIII Collaboration), Nucl. Insrtrum. Meth. **A 614**, 345 (2010).

[7] C. Zhang for BEPC BEPCII Teams, Performance of the BEPC and progress of the BEPCII, in Proceedings of APAC, 2004, pp. 15C19, Gyeongju, Korea.

[8] D. M. Asner *et al.*, Int. J. Mod. Phys. **A 24**, supp (2009).

[9] Z. Y. Wang *et al.* BESIII analysis memo, "Determination of the number of ψ' in 2012".

[10] S. Agostinelli *et al.* (GEANT4 Collaboration), Nucl. Instrum. Meth. **A 506**, 250 (2003).

[11] Z. Y. Deng *et al.* , High Energy Phys. Nucl. Phys. **30**, 371 (2006).

[12] S. Jadach, B. F. L. Ward and Z. Was, Comput. Phys. Commun. **130**, 260 (2000);
S. Jadach, B. F. L. Ward and Z. Was, Phys. Rev. **D 63**, 113009 (2001).

[13] D. J. Lange *et al.*, Nucl. Instrum. Meth. **A 462**, 1 (2001);
R. G. Ping, Chin. Phys. **C 32**, 243 (2008).

[14] J. C. Chen, G. S. Huang, X. R. Qi, D. H. Zhang, and Y. S. Zhu, Phys. Rev. **D 62**, 034003 (2000).

[15] W. D. Li, H. M. Liu *et al.*, in Proceedings o f CHEP06, Mumbai, India, 2006 edited by Sunanda Banerjee (Tata Institute of Fundamental Research , Mumbai, 2006).

[16] R. G. Ping, BESIII DocDB-doc-18-v1 (2007).

[17] G. Punzi, eConf C030908, MODT002 (2003), arXiv:physics/0308063 [physics].

[18] M. Ablikim *et al.* (BESIII Collaboration),Phys. Rev. **D 85**, 092012 (2012).

[19] M. Ablikim *et al.* (BESIII Collaboration),Phys. Rev. **D 83**, 112005 (2011).

[20] M. Ablikim *et al.* (BESIII Collaboration),Phys. Rev. **D 81**, 052005 (2010).

[21] M. Ablikim *et al.* (BESIII Collaboration), Chin. Phys. **C 42**, 023001 (2018).

[22] https://docbes3.ihep.ac.cn/~charmoniumgroup/index.php/XYZProposal#The_helix_correction_factors

[23] K. Stenson, arXiv:physics/0308063 [physics].

[24] X. X. Liu, X. R. Lyu, and Y. S. Zhu, Chin. Phys. **C 39**, 604 113001 (2015).

[25] M. Ablikim *et al.* (BESIII Collaboration), Phys. Rev. D **83**, 112009 (2011).